Size-dependent permittivity and intrinsic optical anisotropy of nanometric gold thin films: a density functional theory study

Slimane Laref,[1] Jiangrong Cao,[2] Abu Asaduzzaman,[1] Keith Runge,[1] Pierre Deymier,[1] Richard W. Ziolkowski,[3] Mamoru Miyawaki,[2] and Krishna Muralidharan[1,*]

[1]*Department of Material Science and Engineering, University of Arizona, 1235 E. James E. Roger Way, Tucson, AZ 85721, USA*

[2]*Optics Research Laboratory, Canon U.S.A. Inc., 9030 S. Rita Road, Tucson, AZ 85747, USA*

[3]*Department of Electrical and Computer Engineering, 1230 E. Speedway Blvd, Tucson, AZ 85721, USA*

[*]*krishna@email.arizona.edu*

Abstract: Physical properties of materials are known to be different from the bulk at the nanometer scale. In this context, the dependence of optical properties of nanometric gold thin films with respect to film thickness is studied using density functional theory (DFT). We find that the in-plane plasma frequency of the gold thin film decreases with decreasing thickness and that the optical permittivity tensor is highly anisotropic as well as thickness dependent. Quantitative knowledge of planar metal film permittivity's thickness dependence can improve the accuracy and reliability of the designs of plasmonic devices and electromagnetic metamaterials. The strong anisotropy observed may become an alternative method of realizing indefinite media.

OCIS codes: (160.4670) Optical materials; (310.0310) Thin films; (250.5403) Plasmonics.

References and links

1. J. L. West and N. J. Halas, "Engineered nanomaterials for biophotonics applications: Improving sensing, imaging, and therapeutics," Annu. Rev. Biomed. Eng. **5**(1), 285–292 (2003).
2. H. A. Atwater and A. Polman, "Plasmonics for improved photovoltaic devices," Nat. Mater. **9**(3), 205–213 (2010).
3. M. Hochberg, T. Baehr-Jones, C. Walker, and A. Scherer, "Integrated plasmon and dielectric waveguides," Opt. Express **12**(22), 5481–5486 (2004).
4. C. Dellagiacoma, T. Lasser, O. J. F. Martin, A. Degiron, J. J. Mock, and D. R. Smith, "Simulation of complex plasmonic circuits including bends," Opt. Express **19**(20), 18979–18988 (2011).
5. V. G. Veselago, "The electrodynamics of substances with simultaneously negative values of ε and μ," Sov. Phys. Usp. **10**(4), 509–514 (1968).
6. J. B. Pendry, A. J. Holden, D. J. Robbins, and W. J. Stewart, "Magnetism from conductors and enhanced nonlinear phenomena," IEEE Trans. Microw. Theory Tech. **47**(11), 2075–2084 (1999).
7. R. A. Shelby, D. R. Smith, and S. Schultz, "Experimental verification of a negative index of refraction," Science **292**(5514), 77–79 (2001).
8. J. A. Scholl, A. L. Koh, and J. A. Dionne, "Quantum plasmon resonances of individual metallic nanoparticles," Nature **483**(7390), 421–427 (2012).
9. P. B. Johnson and R. W. Christy, "Optical constants of the noble metals," Phys. Rev. B **6**(12), 4370–4379 (1972).
10. J. H. Weaver, C. Krafka, D. W. Lynch, and E. E. Koch, *Optical Properties of Metals II: Noble Metals, Aluminum, Lanthanides, and Actinides* (ZAED, 1981).
11. J. Valentine, S. Zhang, T. Zentgraf, E. Ulin-Avila, D. A. Genov, G. Bartal, and X. Zhang, "Three-dimensional optical metamaterial with a negative refractive index," Nature **455**(7211), 376–379 (2008).
12. U. Kreibig and C. V. Fragstein, "The limitation of electron mean free path in small silver particles," Z. Phys. **224**(4), 307–323 (1969).
13. U. Kreibig and M. Vollmer, *Optical Properties of Metal Clusters* (Springer, 1995).
14. Y. He and T. Zeng, "First-principle study and model of dielectric functions of silver nanoparticles," J. Phys. Chem. C **114**(42), 18023–18030 (2010).

#177826 - $15.00 USD Received 11 Oct 2012; revised 12 Apr 2013; accepted 15 Apr 2013; published 7 May 2013

15. K. Glantschnig and C. Ambrosch-Draxl, "Relativistic effects on the linear optical properties of Au, Pt, Pb and W," New J. Phys. **12**(10), 103048 (2010).
16. J. Harl, G. Kresse, L. D. Sun, M. Hohage, and L. Zeppenfeld, "Ab initio reflectance difference spectra of the bare and adsorbate covered Cu(110) surfaces," Phys. Rev. B **76**(3), 035436 (2007).
17. J. Yan, K. W. Jacobsen, and K. Y. Thygesen, "First principles study of surface plasmons on Ag(111) and H/Ag(111)," Phys. Rev. B **84**(23), 235430 (2011).
18. J. C. M. Garnett, "Colours in metal glasses and in metallic films," Phil. Trans. Roy. Soc. London A **203**(359-371), 385–420 (1904).
19. D. R. Smith and D. Schurig, "Electromagnetic Wave Propagation in Media with Indefinite Permittivity and Permeability Tensors," Phys. Rev. Lett. **90**(7), 077405 (2003).
20. Z. Jacob, L. V. Alekseyev, and E. Narimanov, "Optical hyperlens: Far-field imaging beyond the diffraction limit," Opt. Express **14**(18), 8247–8256 (2006).
21. Z. Liu, H. Lee, Y. Xiong, C. Sun, and X. Zhang, "Far-field optical hyperlens magnifying sub-diffraction-limited objects," Science **315**(5819), 1686 (2007).
22. H. N. S. Krishnamoorthy, Z. Jacob, E. Narimanov, I. Kretzschmar, and V. M. Menon, "Topological transitions in metamaterials," Science **336**(6078), 205–209 (2012).
23. G. Onida, W. G. Schmidt, O. Pulci, M. Palummo, A. Marini, C. Hogan, and R. Del Sole, "Theory for modeling the optical properties of surfaces," Phys. Status Solidi **188**(4), 1233–1242 (2001) (a).
24. G. Onida, L. Reining, and A. Rubio, "Electronic excitations: density-functional versus many-body Green's-function approaches," Rev. Mod. Phys. **74**(2), 601–659 (2002).
25. G. Kresse and J. Furthmuller, "Efficiency of ab-initio total energy calculations for metals and semiconductors using a plane-wave basis set," J. Comput. Mater. Sci **6**(1), 15–50 (1996).
26. G. Kresse and J. Furthmüller, "Efficient iterative schemes for ab initio total-energy calculations using a plane-wave basis set," Phys. Rev. B Condens. Matter **54**(16), 11169–11186 (1996).
27. G. Kresse and D. Joubert, "From ultrasoft pseudopotentials to the projector augmented-wave method," Phys. Rev. B **59**(3), 1758–1775 (1999).
28. J. Harl, "The linear response function in density functional theory: Optical spectra and improved description of the electron correlation," Ph.D Dissertation submitted to Universitat Wien (2008).
29. J. P. Perdew, K. Burke, and M. Ernzerhof, "Generalized gradient approximation made simple," Phys. Rev. Lett. **77**(18), 3865–3868 (1996).
30. H. J. Monkhorst and J. D. Pack, "Special points for Brillouin-zone integrations," Phys. Rev. B **13**(12), 5188–5192 (1976).
31. S. Link and M. A. El-Sayed, "Shape and size-dependence of radiative, non-radiative and photothermal properties of gold nanocrystals," Int. Rev. Phys. Chem. **19**(3), 409–453 (2000).
32. M. G. Blaber, M. D. Arnold, and M. J. Ford, "Search for the ideal plasmonic nanoshell: The effects of surface scattering and alternatives to gold and silver," J. Phys. Chem C.Lett **113**(8), 3041–3045 (2009).
33. J. S. Huang, V. Callegari, P. Geisler, C. Brüning, J. Kern, J. C. Prangsma, X. Wu, T. Feichtner, J. Ziegler, P. Weinmann, M. Kamp, A. Forchel, P. Biagioni, U. Sennhauser, and B. Hecht, "Atomically flat single-crystalline gold nanostructures for plasmonic nanocircuitry," Nat Commun **1**(9), 150 (2010), doi:10.1038/ncomms1143.
34. B. J. Wiley, D. J. Lipomi, J. Bao, F. Capasso, and G. M. Whitesides, "Fabrication of surface plasmon resonators by nanoskiving single-crystalline gold microplates," Nano Lett. **8**(9), 3023–3028 (2008).
35. M. Hövel, B. Gompf, and M. Dressel, "Electrodynamics of ultrathin gold films at the insulator-to-metal transition," Thin Solid Films **519**(9), 2955–2958 (2011).
36. X. Wang, K.-P. Chen, M. Zhao, and D. D. Nolte, "Refractive index and dielectric constant transition of ultra-thin gold from cluster to films," Opt. Express **18**(24), 24859–24867 (2010).
37. J. A. Dionne, L. A. Sweatlock, H. A. Atwater, and A. Polman, "Planar metal plasmon waveguides: frequency-dependent dispersion, propagation, localization, and loss beyond the free electron model," Phys. Rev. B **72**(7), 075405 (2005).
38. S. Raza, N. Stenger, S. Kadkhodazadeh, S. V. Fischer, N. Kostesha, A. Jauho, A. Burrows, M. Wubs, and N. A. Mortensen, "Blueshift of the surface plasmon resonance in silver nanoparticles studied with EELS," Nanophotonics **2**(2), 131–138 (2013).

1. Introduction

In the last decade, important advances have been made in fabricating noble-metal based devices for surface plasmon based bio-sensing [1], solar energy harvesting [2], plasmonic circuits [3, 4], as well as for the design of novel metamaterials [5–7]. These devices rely on exploiting the negative permittivity of noble-metals in nanoscale systems for appropriate plasmonic and optical applications, and the ability to design these devices requires an intimate knowledge of the constituent metals' optical permittivity [8]. Typical approaches to obtaining a material's permittivity include using the values either from the literature of inverted optical measurements [9, 10], or from their corresponding phenomenological Drude-model fits. While these ad hoc approaches are reasonable for bulk or bulk-like metallic-systems, they are

#177826 - $15.00 USD Received 11 Oct 2012; revised 12 Apr 2013; accepted 15 Apr 2013; published 7 May 2013

not guaranteed to capture the size-dependent variations of the permittivity once the material's dimensions become nanometric, and empirical adjustments to theoretical estimations are often necessary to match experimental observations. Frequently used adjustments include increasing the Drude model's scattering frequency by a fitting factor [11] or by an empirical size dependent collision frequency formula [12, 13]. The justification for such empirical adjustments is either additional surface scattering induced losses or nonlocal effects, without the knowledge of the exact values of the adjustment parameter(s).

A welcome alternative to the above empirical approaches includes theoretically rigorous electronic-structure methods such as density functional theory (DFT) that have been successfully implemented to study the optical properties of noble-metal systems [14–17]. Employing such methods is immensely beneficial, especially when examining the optical properties of nanoscale systems, and can, in principle, lead to a parameter-free bottom-up modeling and design of photonic and plasmonic devices.

Towards this end, in this work, we report on DFT-based estimations of the optical permittivity of stand-alone, very-thin gold films. Specifically, we study thin films that are up to 30 atomic-layers thick (~7 nm) in the (111) orientation and compare and contrast the differences in the in-plane (i.e., parallel to the film-surface) and out-of-plane (i.e., perpendicular to the film-surface) permittivities as a function of film-thickness for each case, especially at near-infrared (NIR) and visible frequencies. A key distinction from previously reported DFT works [14–17] is the fact that we pay special attention to the interplay between the size and the permittivity of planar gold films. This is of particular technological relevance, given that patterned planar metal films are the basic building blocks for the majority of current plasmonic circuits and optical metamaterials, and little is known about the differences between a nanometric metal film's permittivity and that of a bulk metal.

The obtained results show that the permittivity of the gold thin films under study deviate significantly from their corresponding bulk value. Equally importantly, these thin films exhibit an intrinsic size-dependent optical anisotropy, characterized by a change in the sign of the in-plane versus out-of-plane components of the real part of the permittivity in the NIR spectrum. Furthermore, by characterizing the electronic transitions that govern the permittivity of gold thin films, we demonstrate that there are intrinsic differences in the mechanisms that lead to optical anisotropy in stand-alone gold films, especially when compared to multilayer hyperbolic metamaterials or indefinite media [18–22]. The observed thickness dependence and anisotropy in the permittivity can lead to better accuracy of the electromagnetic (EM) designs of plasmonic devices and optical metamaterials. In addition, such stand-alone gold films may become an alternative method of achieving indefinite media without constructing stacked geometry-based metamaterial structures.

2. Models and methods

DFT based on the Kohn-Sham formulations has become the method of choice to model the ground-state properties of materials from first principles. Obtaining optical properties from DFT, requires going beyond the ground-state properties to include information about electronic excitations. A number of schemes [23] exist for describing electronic excitations including the independent particle approximation (IPA), time-dependent DFT (TD-DFT) and many-body perturbation theory methods [24]. In particular, both IPA with appropriate relativistic corrections [15] and TD-DFT [17] approaches have been successfully implemented for examining the optical permittivity of many metallic systems. Here, we apply IPA, where the permittivity of the material is calculated by evaluating direct electronic transitions between occupied and higher-energy unoccupied electronic states as obtained from the underlying electronic band-structure.

The Vienna Ab initio Simulation Package (VASP) [25, 26] using the scalar-relativistic projector augmented wave (PAW) method [27] and the PBE-GGA exchange-correlation functional [28], is employed within the IPA framework for evaluating the real (Re) and

#177826 - $15.00 USD Received 11 Oct 2012; revised 12 Apr 2013; accepted 15 Apr 2013; published 7 May 2013

imaginary (Im) components of the optical permittivity tensor. The optical permittivity consists of interband (ε^{inter}) and Drude-like free-electron intraband (ε^{intra}) contributions. Equation (1) expresses the imaginary part of the interband contributions (from which the real part can then be calculated via the Kramers-Kronig relations), while the intraband contributions are given in Eq. (2) as discussed by Harl [28].

$$Im\left[\varepsilon^{inter}_{x_1x_2}(\omega)\right]=\frac{8\pi^2e^2}{V}\lim_{q\to 0}\frac{1}{|q|^2}\sum_{m,n}2f_{nk}\langle u_{m,k+q\hat{x}_1}|u_{n,k}\rangle\langle u_{n,k}|u_{m,k+q\hat{x}_2}\rangle\times \left[\delta\left(\xi_{m,k+q}-\xi_{n,k}+\hbar\omega\right)-\delta\left(\xi_{m,k+q}-\xi_{n,k}-\hbar\omega\right)\right] \tag{1}$$

Here, x_1, x_2 represent the different Cartesian directions, the delta function satisfies energy conservation for a direct electronic transition between two single particle energies, ξ, belonging to two different energy bands, m and n, in the limit of a vanishing photon wave-vector q for a given k-point in the first Brillouin zone. The quantity u represents the component of the Bloch wave function exhibiting the periodicity of the underlying lattice, V is the volume of the simulated unit cell, and f corresponds to the occupation number of a particle energy ξ. $Re[\varepsilon^{inter}(\omega)]$ is obtained from a Kramers-Kronig transform of the corresponding imaginary part calculated from Eq. (1). The corresponding intraband contributions to the real and imaginary parts of the permittivity are given by the Drude model forms:

$$Re\left[\varepsilon^{intra}(\omega)\right]=1-\frac{\omega_p^2}{\omega^2+\Gamma^2};\quad Im\left[\varepsilon^{intra}(\omega)\right]=\frac{\Gamma\omega_p^2}{\omega^3+\omega\Gamma^2} \tag{2}$$

where Γ represents a life-time broadening obtained either from a higher-order calculation or experiments, while ω_p represents the intraband free electron plasma frequency tensor, as given in Eq. (3).

$$\omega_p^2(x_1,x_2)=-\frac{4\pi e^2}{V}\sum_{n,k}2\frac{\partial f(\xi_n)}{\partial\xi_n}\left(\frac{\partial\xi_n(k)}{\partial k}\hat{x}_1\right)\left(\frac{\partial\xi_n(k)}{\partial k}\hat{x}_2\right) \tag{3}$$

Note that fully occupied bands do not contribute to the intraband plasma frequency. Finally, it should be noted that the interband contribution to the permittivity that arises due to electronic transitions between states separated by low energy differences can be correlated to an associated intraband contribution via the f-sum rule, which states that the integrated intraband and interband contributions should sum up to a fixed value [29].

3. DFT computational details

Both bulk and thin-film properties of gold were calculated on the DFT primitive cell, with a 12 × 12 × 12 (for bulk) and 12 × 12 × 1 (thin-film) Monkhorst-Pack-set [30]. Convergence of the total energy was ensured by setting the plane-wave cutoff for the wavefunction expansion (and for that of the charge density) to 400 and 645 eV for the bulk and (thin-films respectively. Supercells consisting of 6-atomic layer thick (~1.2 nm) to 30-atomic-layer thick (~7.03 nm) thin-film slabs were simulated with the basal plane represented by a 1 × 1 cell. A sufficiently thick vacuum-layer in the directions perpendicular to the (111) films was introduced to prevent spurious interactions between periodic replicas. It was seen that for vacuum-layer thicknesses ≥ 11 Å, there was no effect on the energy and optical properties of the thin-films under study. The atomic positions were relaxed by minimizing the forces according to a quasi–Newton algorithm. For all cases, the thin film layers were relaxed until forces on the atoms were lower than 0.001 eV/Å. For optical permittivity calculations a k-point grid corresponding to 41 × 41 × 41 (for bulk) and 41 × 41 × 1 (for thin film) was chosen

#177826 - $15.00 USD Received 11 Oct 2012; revised 12 Apr 2013; accepted 15 Apr 2013; published 7 May 2013

to ensure a sufficient description of the optical permittivity. For the integration over the Brillouin zone, we used the first order Methfessel-Paxton method with a value of 0.2 eV. A lifetime broadening of 0.018 eV for the intraband transitions was used, which is consistent with [31, 32]. The obtained permittivities were suitably renormalized to exclude the vacuum region and, thereby, enabling appropriate comparisons between the different-sized thin films.

4. Permittivity of bulk Gold

Before discussing the permittivity variations as a function of film-thickness, an initial check was carried out to confirm that the adopted computational procedure could accurately model the optical properties of bulk gold. Figure 1 illustrates the real and imaginary parts of the optical permittivity predicted by the DFT method in comparison to the available experimental data that is widely adopted in literature [9, 10]. As evident from Fig. 1, the predicted DFT data compares well with the experimental results. Moreover, the DFT-calculated intraband plasma frequency ($\hbar\omega_p$) equaling 8.65 eV matches well with the 8.9 eV experimental value [9].

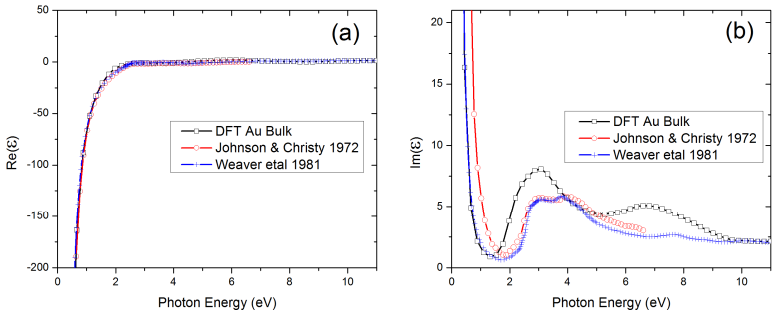

Fig. 1. The real (a) and imaginary (b) part of the permittivity of bulk gold as predicted by the adopted DFT method, in comparison with data from standard literature.

The intraband and interband contributions to the total permittivity are shown in Figs. 2(a) and 2(b). Characteristic features in the visible spectrum such as the peak in the imaginary part of the permittivity (Fig. 2(b)) at around 3 eV are captured by our adopted method, in agreement with experiments. This peak is attributed to electronic transitions occurring from the d-band to the p-band close to the Fermi level at around the X and the L points, as illustrated in Fig. 2(c). A more detailed analysis of the oscillator strengths governing the various electronic transitions responsible for the optical permittivity has been discussed previously [15]. It is worth noting that the predicted optical response compares well with the above work as seen in the appearance of prominent peaks in the imaginary part at around 7 eV, 13 eV and 20 eV. In [15], the full-potential linearized augmented plane wave (LAPW) method is used to represent the Kohn-Sham orbitals, while in this work, PAW is employed. Further, spin-orbit effects were explicitly included in [15]; these lead to minor deviations in the exact location of the above peaks. Nevertheless, the essential features in the permittivity are captured well in our work, confirming the reliability of our DFT approach.

#177826 - $15.00 USD Received 11 Oct 2012; revised 12 Apr 2013; accepted 15 Apr 2013; published 7 May 2013

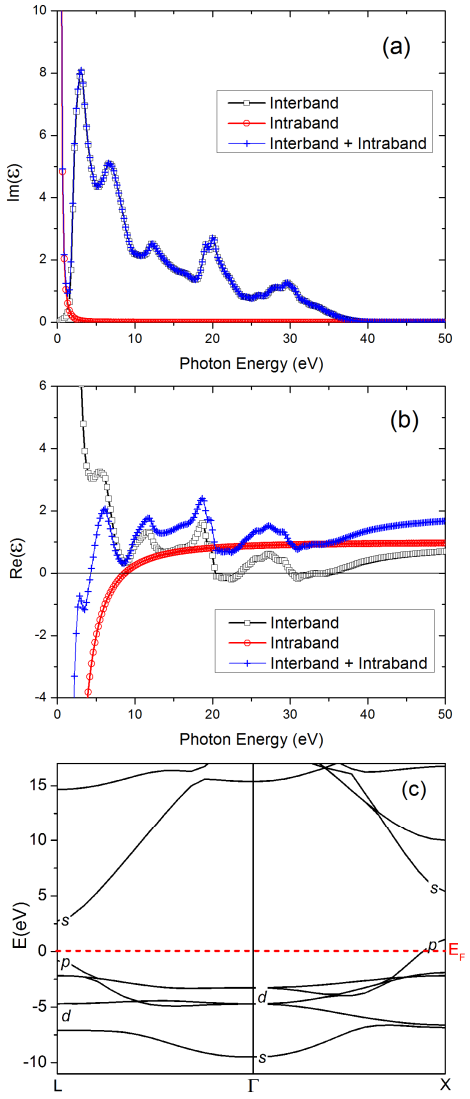

Fig. 2. The interband and intraband contributions to the imaginary (a) and real (b) parts of the permittivity of bulk gold, as evaluated from the adopted DFT method. The electronic band structure of bulk gold along the ΓX and ΓL directions as calculated from the adopted DFT method (c). The red dotted line in (c) indicates the Fermi-level. The labels s,p,d represent the dominant orbital characters of the bands at their high-symmetry points.

5. Permittivity of Gold thin films

In this work, only pristine, atomically flat thin films are considered. The focus is on the development of an important fundamental understanding on the effect of the thickness on the permittivity tensor. To achieve this, we consider (111) nanometric thin films in the thickness range (1-7 nm). The films computed here model the condition of single crystalline gold films as recently demonstrated experimentally [33, 34], which are different from the poly-crystalline thin films with isolated islands [35, 36].

In Fig. 3(a), we illustrate the variation in the in-plane plasma frequency as a function of the film-thickness. The fact that the plasma frequency increases with increasing thickness suggests that the thinner samples deviate more in their ‘metallic’ behavior as compared to

#177826 - $15.00 USD Received 11 Oct 2012; revised 12 Apr 2013; accepted 15 Apr 2013; published 7 May 2013

bulk; and, equally importantly, that the finiteness in the perpendicular dimension affects the in-plane optical response. In Figs. 3(b) and 3(c), we depict the variations in the real and imaginary in-plane permittivity ($\varepsilon^{in\text{-}plane}$) components as functions of the photon energy for different thicknesses of the (111) thin films. There are discernible differences with respect to the bulk permittivity, especially for films thinner than 4 nm, which are attributed to the variations in the plasma frequency and to the offsetting interband contributions. These differences are shown in Fig. 3(d) for select systems. In particular, the interband contributions demonstrate a peak at around 1.0 eV in Im($\varepsilon^{in\text{-}plane}$) in Fig. 3(d), which is absent for the bulk. This peak shifts further to lower energies as the thickness increases. These trends are directly related to the underlying band-structure shown in Figs. 4(a)-4(b), where the band-structures in the ΓX direction for the 3.6 nm and 7 nm thick gold thin films are given in comparison with the equivalent bulk-system. For the thin films, the relative position of the top of the d-band at the X-point is shifted with respect to the bulk-system value, and this shift depends on the film thickness. Furthermore, the p-band is now present below the Fermi-level for the thin-films, which is not the case for the bulk system. The electronic transitions between the d-band and the p-band states lead to the shift of the 1eV interband peak in Fig. 3(d).

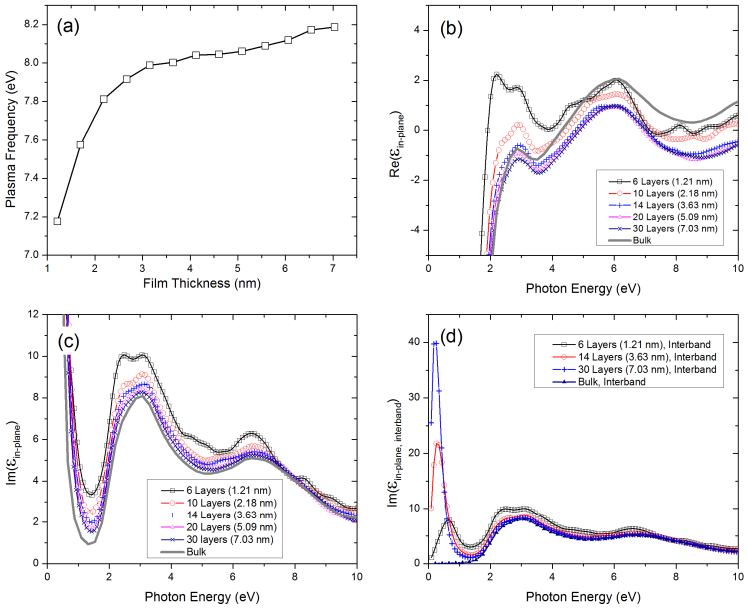

Fig. 3. Variations in (a) In-plane plasma frequency, (b) the real part of the in-plane permittivity, and (c) imaginary part of the in-plane permittivity as a function of lateral film-thickness. Note that the real part of the permittivity for all cases decreases monotonically below 2 eV and, hence, is not highlighted in (b). (d) represents the interband contributions to the imaginary part of the in-plane permittivity for the indicated select thin-film systems.

From an EM device design point of view, the observed thickness dependences in Fig. 3 are significant. In addition to the in-plane plasma frequency shifts (Fig. 3(a)), the Re($\varepsilon^{in\text{-}plane}$) values for photon energy below 3.2 eV (representing the visible and infrared spectra) in Fig. 3(b) for instance, show deviations from the bulk value by more than 50% with respect to the Re($\varepsilon^{in\text{-}plane}$) = 0 line. These changes are more dramatic than prior empirical Drude model adjustments suggested, for instance, in previous reports [12, 13].

Next, as shown in Figs. 5(a) and 5(b), the effect of the finite-dimension of the thin-films on the out-of-plane permittivity is more pronounced. In particular, the out-of-plane permittivity ($\varepsilon^{out\text{-}of\text{-}plane}$) exhibits significant departure from both the bulk and the in-plane counterparts, especially at low energies corresponding to the NIR (i.e., photon energies below

#177826 - $15.00 USD Received 11 Oct 2012; revised 12 Apr 2013; accepted 15 Apr 2013; published 7 May 2013

1.7eV in Figs. 5(a)-5(b)). By comparing Fig. 3(b) and Fig. 5(b), one can see a distinct anisotropy in the permittivity of stand-alone gold thin films, i.e., there is a clear sign-flip between the Re($\varepsilon^{in\text{-}plane}$) and Re($\varepsilon^{out\text{-}of\text{-}plane}$) values. This sign flip is a result of the fact that the out-of-plane optical response is primarily dominated by the interband transitions, as discussed above, while the intraband contributions are negligible for the out-of-plane optical response. The latter is due to the confined dimension in the out-of-plane direction. The intrinsic evolution of the electronic-structure as a function of the film-thickness gives rise to the observed anisotropic properties, which fundamentally differs from the anisotropy that arises from the effective medium theory (EMT) effects in hyperbolic metamaterials and indefinite media metamaterials [18–22].

Finally, while not discussed in this paper, we would like to point out that similar behavior in the plasma frequency variations and permittivity anisotropy was observed for (100) gold thin films of comparable dimensions.

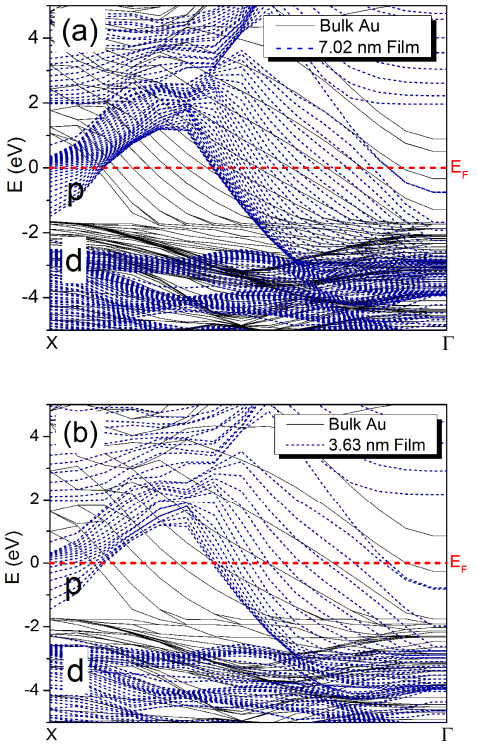

Fig. 4. The band structure for (a) 7.02 nm, thick and (b) 3.63 nm (111) gold thin-films in the ΓX direction.

#177826 - $15.00 USD Received 11 Oct 2012; revised 12 Apr 2013; accepted 15 Apr 2013; published 7 May 2013

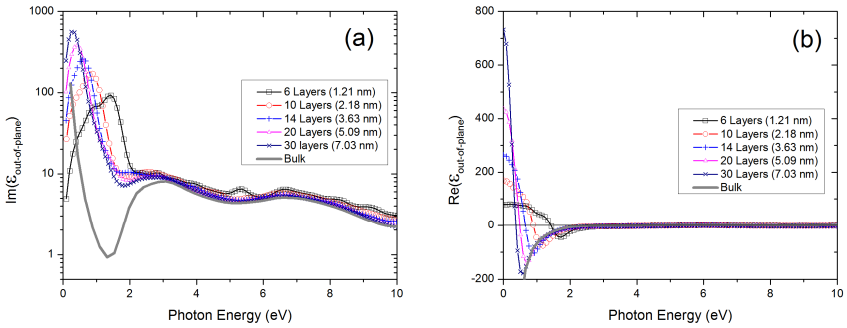

Fig. 5. (a) Imaginary part and (b) real part of the out-of-plane permittivity as a function of the film-thickness.

6. Guided surface plasmon modes on an anisotropic Gold thin film

Based on the above-discussed DFT observations and from the perspective of plasmonic devices and EM metamaterials, it is clear that the spectral region of particular interest is where the variation of the anisotropy is significant, as seen in the sign-flip of $Re(\varepsilon_{zz})$, c.f., the low photon energy portion of Fig. 5(b). Here, 'zz' represents the out-of-plane permittivity component. A sign-flip in $\mathrm{Re}(\varepsilon_{zz})$ may result in the loss of the material's ability to sustain a guided surface plasmon mode confined at a single interface between metal and dielectric media, because it is known that a single interface between two positive isotropic Re(ε) media does not support any confined and guided modes.

To look into this possibility, we next studied the evolution of the surface plasmon mode propagating along a single interface between a negative Re(ε) plasmonic metal and a positive Re(ε) media. These highly confined modes are the basic building block of all plasmonic devices.

We first deduced an analytical form of the guided surface modes at an interface between an arbitrary anisotropic material and a regular dielectric media (e.g., air, glass, etc.). The interface problem that we have solved is illustrated in Fig. 6, where the z-axis is the direction perpendicular to the interface, and the x-axis is the propagation direction of the guided modes being solved.

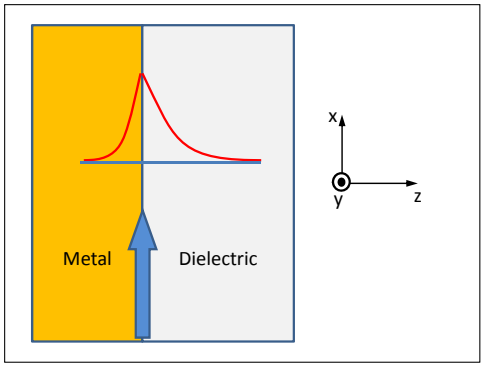

Fig. 6. An illustration of the surface plasmon guided mode being investigated at the interface between a metal and a dielectric material

The dielectric media in Fig. 6 is represented by a real valued permittivity ε_d. The corresponding metal media is represented by a complex valued, bi-axial permittivity tensor:

#177826 - $15.00 USD Received 11 Oct 2012; revised 12 Apr 2013; accepted 15 Apr 2013; published 7 May 2013

$$\overline{\overline{\varepsilon}}_m = \begin{bmatrix} \varepsilon_{xx} & 0 & 0 \\ 0 & \varepsilon_{yy} & 0 \\ 0 & 0 & \varepsilon_{zz} \end{bmatrix} \tag{4}$$

First, the anisotropic tensor components ε_{xx}, ε_{yy} and ε_{zz} are set all equal and are represented by a basic Drude form with ω_p = 8.65 eV and γ = 0.018 eV. The resulting dispersion of the classical guided surface plasmon mode between this plasmonic material and dielectric (ε_d = 1.0 in this case) is obtained and plotted it as the blue squares in Figs. 7(a) and 7(b).

Then, by flipping the sign of Re(ε_{zz}), we obtained a solution for the guided surface plasmon mode at the surface of an anisotropic metal. The resulted guided mode solution is plotted as the red dots in Figs. 7(a) and 7(b).

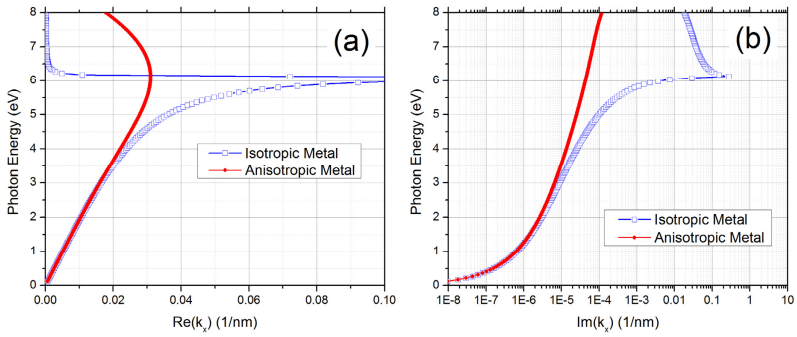

Fig. 7. (a) Real part of the wave number of the of guided modes at the surface of an isotropic metal (blue squares) and an anisotropic metal (red dots); (b) imaginary part of the wave number of the guided modes at the surface of an isotropic metal (blue squares) and an anisotropic metal (red dots).

Through Figs. 7(a) and 7(b), we found that the confined surface plasmon mode still exists, even when the Re(ε_{zz}) becomes positive, and the wave number of the surface plasmon mode only deviates slightly from its classical value in low photon energy region. However, when the photon energy is increased towards the cut-off level, e.g., near 6.1 eV in Figs. 7(a) and 7(b), the difference becomes pronounced.

Next, a finite thickness metal film sandwiched between two identical dielectric media was investigated. The structure and the two guided (even and odd) surface plasmon modes are illustrated in Fig. 8.

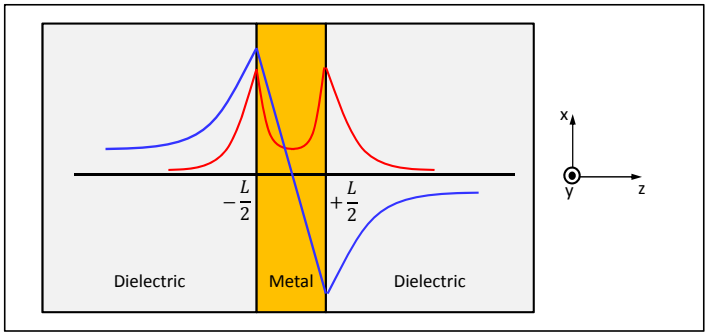

Fig. 8. An illustration of the two surface plasmon guided modes on a finite thickness metal film sandwiched between two identical dielectric media. The red and blue curves illustrate the electrical field profile of the symmetric (even) and antisymmetric (odd) modes, respectively.

#177826 - $15.00 USD Received 11 Oct 2012; revised 12 Apr 2013; accepted 15 Apr 2013; published 7 May 2013

To test the impact of the anisotropic permittivity in the metal, the dispersion relations of the two guide modes were obtained analytically. They are given, respectively, by the expressions:

$$\varepsilon_{xx} - i\tan\left(i\sqrt{\frac{\varepsilon_{xx}}{\varepsilon_{zz}}k_x^2 - \varepsilon_{xx}k_0^2}\,\frac{L}{2}\right)\frac{\varepsilon_d\sqrt{\frac{\varepsilon_{xx}}{\varepsilon_{zz}}k_x^2 - \varepsilon_{xx}k_0^2}}{\sqrt{k_x^2 - \varepsilon_d k_0^2}} = 0 \tag{5}$$

$$\varepsilon_{xx} + i\cot\left(i\sqrt{\frac{\varepsilon_{xx}}{\varepsilon_{zz}}k_x^2 - \varepsilon_{xx}k_0^2}\,\frac{L}{2}\right)\frac{\varepsilon_d\sqrt{\frac{\varepsilon_{xx}}{\varepsilon_{zz}}k_x^2 - \varepsilon_{xx}k_0^2}}{\sqrt{k_x^2 - \varepsilon_d k_0^2}} = 0 \tag{6}$$

They were deduced by matching boundary conditions at the interfaces: $z = -\frac{L}{2}$ and $z = +\frac{L}{2}$, illustrated in Fig. 8. Here, L is the metal film thickness; k_0 is the vacuum wave number of the guided wave; ε_d is the permittivity of the dielectric claddings; ε_{xx} and ε_{zz} are, respectively, the complex valued in-plane and out-of-plane permittivities of the metal film; and k_x is the complex valued tangential wave number of the guided mode. In the special case when the metal has an isotropic permittivity, i.e., when $\varepsilon_{xx} = \varepsilon_{zz}$, the dispersion relations Eq. (5) and Eq. (6) reduce to those given in [37].

Next, a 20 atomic layer (111) Au film (5.09 nm thick) was assumed to be sandwiched by dielectrics with $\varepsilon_d = 2.25$. The even and odd guided mode dispersion relations then were obtained under two alternative metal permittivities: (1) anisotropic (i.e., ε_{xx} and ε_{zz} were set to be the exact DFT output values for the 5.09 nm thick film as presented in Figs. 3(b)-3(c) and Figs. 5(a)-5(b), and (2) isotropic (i.e., both the in-plane and out-of-plane permittivities of the metal were set equal to the DFT computed ε_{xx} values for the 5.09 nm thick film). Figures 9(a)-9(d) plots the results obtained. Figure 9(a) shows the antisymmetric mode is mostly squeezed out of the metal region and exists primarily in the dielectric cladding for this thin film thickness. This observation is consistent with the results reported in [37] when the silver film thickness was reduced from 50 nm to 12 nm. Figures 9(c) and 9(d) show the symmetric mode is still significantly confined in the metal, even though the metal thickness is as thin as 5.09 nm. Moreover, when comparing the anisotropic and isotropic results, it is clear that the DFT-predicted anisotropy does have a significant impact on the dispersion characteristics of the symmetric guided mode.

#177826 - $15.00 USD Received 11 Oct 2012; revised 12 Apr 2013; accepted 15 Apr 2013; published 7 May 2013

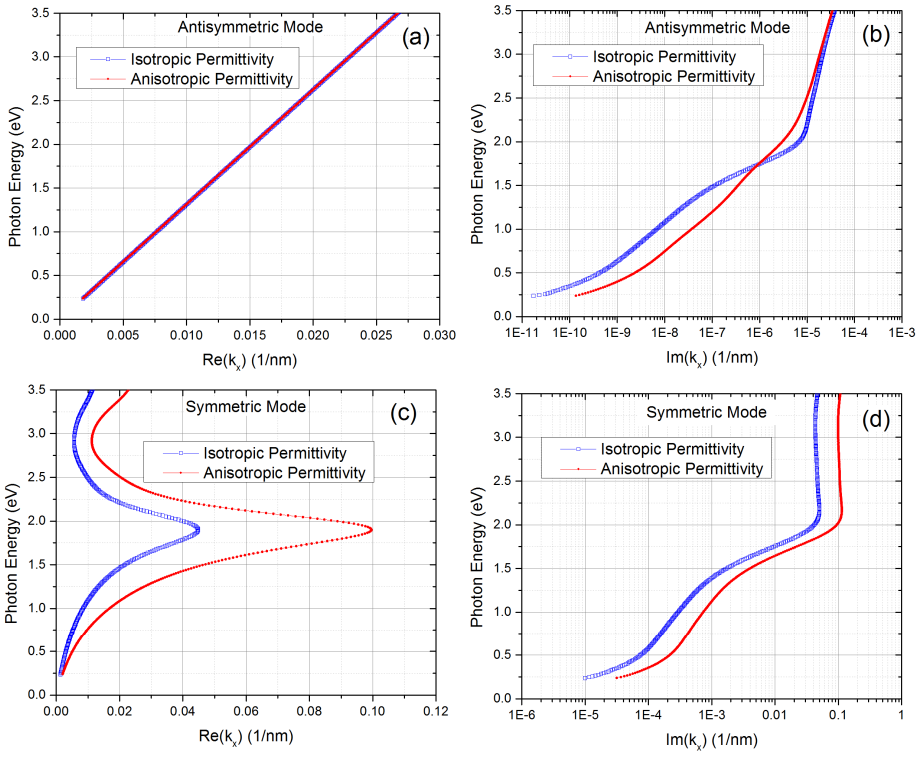

Fig. 9. Dispersion characteristics for the two guided modes in the structure illustrated in Fig. 8. The empty squares plot the solutions using the isotropic permittivity in the metal. The solid red circles plot the solutions using the anisotropic permittivity in the metal. (a) and (b) show the antisymmetric mode. (c) and (d) show the symmetric mode. (a) and (c) show the real part of the wave number component along the interface; (b) and (d) show its imaginary part.

7. Conclusion

Using rigorous DFT calculations, we have examined and characterized the size dependent variations in the optical permittivity of nanometric (111) gold thin films. Both in-plane and out-of-plane permittivity components were found to be thickness dependent. Further, significant anisotropy in the in-plane and out-of-plane permittivities was observed, and the real part of the out-of-plane permittivity was characterized by a sign-flip in the NIR spectrum, which is interestingly, similar to the experimental results [8,38] suggested, where quantum-confinement effects were responsible for a sign-flip in a silver nanoparticle's permittivity. In conclusion, the observations reported in this work are particularly important, since the quantitative knowledge of planar metal film permittivity's thickness dependence can improve the accuracy and reliability of the EM designs of plasmonic devices and optical metamaterials [e.g 1–7.]. The strong anisotropy observed is of significance and can help in realizing indefinite media using stand-alone nanometric gold thin films.

Acknowledgments

Authors (S.L, K.M, R.W.Z, P.D and K.R) would like to acknowledge Canon USA Inc. for their financial support. J.C. would like to acknowledge fruitful discussions with Aihiko Numata.

#177826 - $15.00 USD Received 11 Oct 2012; revised 12 Apr 2013; accepted 15 Apr 2013; published 7 May 2013